Breaking internal waves on sloping topography: connecting parcel displacements to overturn size, interior-boundary exchanges, and mixing

Victoria Whitley[a] and Jacob Wenegrat[a,b]

[a] *Applied Mathematics & Statistics, and Scientific Computation Program, University of Maryland, College Park*

[b] *Department of Atmospheric and Oceanic Science, University of Maryland, College Park*

Corresponding author: Victoria Whitley, whitleyv@umd.edu

ABSTRACT: Internal waves impinging on sloping topography can generate mixing through the formation of near-bottom bores and overturns in what has been called the 'internal swash' zone. Here we investigate the mixing generated during these breaking events, and the subsequent ventilation of the bottom boundary layer, across a realistic non-dimensional parameter space for the ocean using three-dimensional large eddy simulations. Waves overturn and break at two points during a wave period: when the downslope velocity is strongest and during the rapid onset of a dense, upslope bore. From the first overturning bore to the expulsion of fluid into the interior, there is a strong dependence on the length scale defined by the ratio of wave velocity over the background buoyancy frequency, an upper bound on the vertical parcel displacement an internal wave can cause. While this energetically-motivated vertical length scale is often seen in the context of lee wave generation over topography, the results discussed here suggest the same parameter can be used to determine the size of near-boundary overturns, the strength of the ensuing turbulent mixing, and the vertical scale of the along-isopycnal intrusions of fluid ejected from the boundary layer. Consideration of a volume budget of the near-boundary region highlights spatial and temporal variability that must be taken into account when determining the water-mass transformation during this process.

1. Introduction

Internal waves breaking on topography are a significant to many ocean processes. Internal tides impinging on both critical and off-critical topography can result in bottom-enhanced turbulent mixing, and diapycnal upwelling necessary for the closure of the abyssal circulation (Eriksen 1985; Polzin et al. 1997; Slinn and Riley 1998; Kunze et al. 2012; Cyr and van Haren 2016; Chalamalla et al. 2013; van Haren and Gostiaux 2012b). Recent theoretical work and observations suggest upwelling near sloping bottom boundaries may be limited to turbulent Bottom Boundary Layers (BBLs) where the mixing profile allows for convergent turbulent buoyancy fluxes, (Ferrari et al. 2016; Mashayek et al. 2017; Wynne-Cattanach et al. 2023). Exchanges between the stratified interior and the well-mixed BBL associated with breaking internal waves could be a pathway for the restratification of these boundary waters, necessary to maintain an efficient diapycnal process (Armi 1978; van Haren 2023). These breaking events and interior exchanges also allow for the transport and recycling of carbon, oxygen, and nutrients crucial for the ecosystem (Cheriton et al. 2014; Churchill et al. 1988; Bonnin et al. 2006; Cyr and van Haren 2016; McPhee-Shaw et al. 2021). The reflection and possible breaking of internal waves could result in bottom velocities strong enough to resuspend particles on the sea floor in nepheloid layers (Cacchione and Drake 1986), often observed in lake and coastal settings (e.g., McPhee-Shaw 2006; Bonnin et al. 2006; Edge et al. 2021). These nepheloid layers are also observed as intrusions into the interior (Gardner et al. 2017; Thorpe and White 1988), similar to internal wave laboratory experiments and numerical models showing layers of dye ejected from the slope (Nokes and Ivey 1989; Winters 2015).

There has been extensive work done on the generation, and nearby-breaking, of internal waves over topography (Winters and Armi 2013; Sarkar and Scotti 2017). Several parameters have been used to characterize internal waves near topography in the presence of both oscillating and steady barotropic forcing, including the criticality of the slope, the nonlinearity of the resulting wave behavior, and the ability of the flow to overcome obstacles (Winters and Armi 2013; Chalamalla et al. 2013; Sarkar and Scotti 2017; Legg and Klymak 2008; Drazin 1961). When a steady flow is blocked by topography, the length scale given by the steady velocity, U, over the buoyancy frequency, N, represents the thickness of the layer that can continue past the obstacle (Winters and Armi 2013). This results in a new “effective height,” $h_{eff} = U/N$, of the topography and sets the vertical scale for the resulting waves (Winters and Armi 2013; Legg and Klymak 2008).

This ratio is included in the Scorer number, as well, an atmospheric parameter characterizing lee waves (Scorer 1949). The effective height leads to the characterization of the topographic Froude number, $Fr = U/Nh$, where h is the obstacle's height. Nonlinear hydraulic effects can be found in simulations of small Fr, (Sarkar and Scotti 2017; Chalamalla et al. 2013; van Haren 2023), where the height of the obstacle is much larger than the effective height.

While the formation and breaking of lee waves above topography have been extensively modeled and observed, there is also clear evidence of turbulence resulting from remotely forced internal waves reaching sloping boundaries (Aucan et al. 2006; van Haren et al. 2015). The oscillating flow of internal waves up and down the slope results in intermittent overturns and breaking within the phases of the wave period, sometimes described as "swashing" motions (Cyr and van Haren 2016). The overturns tend to occur at the rapid transition between down and upslope flow, as well as during the downslope phase where intensified near-slope velocities result in shear along the slope (Cyr and van Haren 2016; Aucan et al. 2006; Winters 2015; van Haren and Gostiaux 2012b; Gayen and Sarkar 2011). Previous studies have highlighted the nonlinearity found when the slope of the incident internal wave is close to that of the topography, trapping energy near the boundary and resulting in wave breaking and increased dissipation (Nokes and Ivey 1989; Slinn and Riley 1998; Lamb 2014). In a simulation with a low-mode internal tide impinging on a supercritical slope in rotating, stratified fluid, Winters (2015) notes a visual similarity between the length scales of the breaking and expulsion events and a vertical length scale defined similarly to h_{eff} except with velocity scale set by the wave velocity itself, but does not explore this dependence in parameter space. Motivated by these observations and results, this paper focuses on a set of highly-resolved, three-dimensional simulations of internal waves impinging on sloping boundaries, where wave amplitude, stratification, frequency, and criticality are varied, spanning a range of values relevant to the ocean. There is a strong dependence on the vertical effective wave height throughout the breaking process, resulting in subsequent dissipation and boundary-interior exchange scaled by the effective wave height near the slope.

The manuscript is organized as follows. In section 2 we introduce the high-resolution model used to explore the breaking events as well as a description of the parameter space surveyed in this study. In section 3 we describe a characteristic breaking event and introduce the governing scaling found throughout the mixing process. This is followed by an explanation of the mechanism

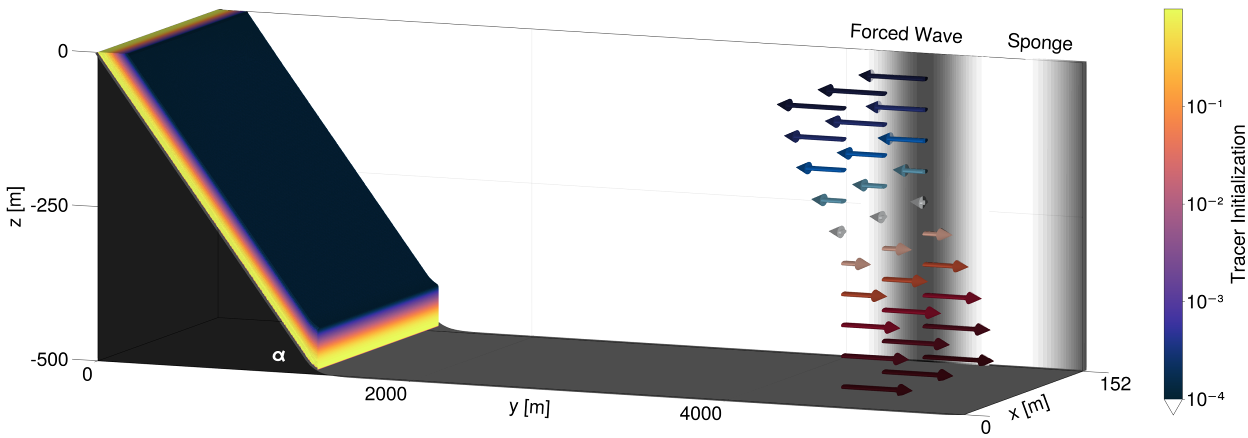

FIG. 1. 3D LES domain set up. Planar topography with slope $\tan\alpha$ shown in black. The location of the forced internal wave is indicated with arrows centered at $y = 4500$, and the gray Gaussian contours behind the arrows. The sponge regions near the right boundary are also marked out with gray contours, representing the amplitude of damping. Contours of the initial hyperbolic tangent condition of the concentration of the tracer are also shown. The tracers are uniformly initialized in the across-slope direction, similar to the topography.

behind the resulting interior and boundary exchange with connections to the previously discussed vertical scaling. Water-mass transformation and diapycnal mixing involved is then analyzed for a representative simulation. Conclusions, and several avenues for future study, are reviewed in section 4.

2. Numerical Model Set Up

To explore the interaction between the BBL and the interior in the presence of breaking internal waves, we use high-resolution Large Eddy Simulations (LES) of internal waves impinging on a planar slope. The incompressible Navier-Stokes equations under the Boussinesq approximation are solved using a non-hydrostatic model in the julia package, *Oceananigans* (Ramadhan et al. 2020). The domain, shown in Fig. 1, is three-dimensional, with size $(L_x, L_y, L_z) = (152, 6500, 500)$ m, with periodicity in the along-isobath (x) direction and uniform grid spacing of $\Delta y = \Delta x = 4$ m and $\Delta z = 2$ m. To test the grid resolution dependency, vertical grid spacing was varied from $\Delta z = 1.5$ m to 6 m, and the horizontal spacing from $\Delta x = \Delta y = 3$ m to 8 m. The chosen grid spacing was

Table 1. Simulation Parameters for Main Reference Set

	Vary V_0		Vary N_0	
h_w [m]	V_0 [ms^{-1}]	N_0^2 [s^{-2}]	V_0 [ms^{-1}]	N_0^2 [s^{-2}]
14.29	0.05	1.23×10^{-5}	0.25	3.06×10^{-4}
28.57	0.10	1.23×10^{-5}	0.25	7.66×10^{-5}
42.86	0.15	1.23×10^{-5}	0.25	3.40×10^{-5}
57.14*	0.20	1.23×10^{-5}	0.25	1.91×10^{-5}
71.43	0.25	1.23×10^{-5}	0.25	1.23×10^{-5}
85.71	0.30	1.23×10^{-5}	0.25	8.51×10^{-6}
100.00**	0.35	1.23×10^{-5}	0.25	6.25×10^{-6}
114.29	0.40	1.23×10^{-5}	0.25	4.79×10^{-6}
128.57	0.45	1.23×10^{-5}	0.25	3.78×10^{-6}
142.86	0.50	1.23×10^{-5}	0.25	3.06×10^{-6}
157.14	0.55	1.23×10^{-5}	0.25	2.53×10^{-6}

*Similar to the values used in Winters (2015)

**Similar to the values observed in van Haren (2006)

found to resolve the Ozmidov length, defined as,

$$L_O = 2\pi\Big(\frac{\bar{\epsilon}}{N_0^3}\Big)^{1/2}, \tag{1}$$

where $\bar{\epsilon}$ is the average dissipation of kinetic energy rate over turbulent regions, ($\epsilon > 10^{-10}$ m^{2}s^{-3}) (Khani 2018). Results discussed in this paper were also found to be qualitatively insensitive to the changes in resolution.

Boundary conditions in the bottom normal direction are no flux on buoyancy and tracers and quadratic drag on momentum. Topography is included in the simulation using a grid-fitted immersed boundary method with the quadratic drag boundary conditions set on each boundary-adjacent cell face. The idealized domain is initialized with a uniform stratification, N_0^2, and constant Coriolis frequency, f, with the ratio, $N_0/f = 10.7$, kept constant over all simulations. The topographic slope is given by $\tan\alpha$. A full list of parameters for the main set of simulations can be found in Tables 1 and 2.

The exchange of fluid between the lower boundary layer and the interior is quantified using a passive tracer initialized along the entire slope boundary using a hyperbolic tangent function

TABLE 2. Constant Simulation Parameters for Main Reference Set

Parameter	Value	Comment
N_0/f	10.7	Chosen for comparison to Winters (2015)
σ/f	2.2	$\sigma/f > 2$, PSI possible
h [m]	500	Height of topography
$\ell[m]$	1406	Length of topography
$\tan\alpha$	0.356	Topographic slope ($\mathrm{d}h/\mathrm{d}\ell$)
γ	1.9	Slope is supercritical ($\tan\alpha/\tan\theta$)

extending 20 m above the slope. This initialization can also be seen in Fig. 1. The immersed boundary method used in Oceananigans was found to conserve the dye for this simulation setup.

In each simulation, mode-1 oscillations are continuously forced in the v momentum equation. The forcing region is determined by a Gaussian centered at $y = 4500$ m, more than 3000 m from the closest point of the slope, as seen in the arrows and gray contours in Fig. 1. The forcing is derived by taking the v component from linear internal wave theory as

$$v(x, y, z, t) = V_0 \cos(ly + mz - \sigma t), \tag{2}$$

with amplitude, V_0, and frequency, σ, specified in each simulation. The horizontal wave number, l, is determined from the dispersion relation for linear internal waves. Simulations were run with mode-1 vertical wave number, $m = \pi/L_z$, representative of an internal tide. Using only the v component was found to be sufficient to set up an oscillating internal wave, with resulting velocities close to the prescribed V_0. Typically, tidal velocities would be a few centimeters per second, although this is varied here from 0.05 ms^{-1} to 0.55 ms^{-1} to span a wide range of the parameter space (Table 1). The wave period, $T_\sigma = 2\pi/\sigma$, from the forced wave, will be used to describe some simulation results. All simulations are run for at least 11 wave periods, with a variable time step between 10^{-4} s and 10 s, as determined by a CFL of 0.5 within the simulation. Diagnostics are calculated every 600 s, or such that there are at least 15 snapshots every wave period. A sponge region is added to all fields along the right boundary of the domain to prevent spurious reflections (sponge region marked with gray contours in Fig. 1).

TABLE 3. Simulation Parameters for Assessing Sensitivity to Wave Frequency, σ, and Criticality, γ

Vary γ						
h_w [m]	V_0 [ms^{-1}]	N_0^2 [s^{-2}]	N/f	σ/f	γ ($\tan\alpha/\tan\theta$)	$\tan\alpha$ (dh/dx)
42.86	0.15	1.23×10^{-5}	10.7	2.8	1.4	0.356
42.86	0.15	1.23×10^{-5}	10.7	5.5	0.6	0.356
128.57	0.45	1.23×10^{-5}	10.7	2.8	1.4	0.356
128.57	0.45	1.23×10^{-5}	10.7	5.5	0.6	0.356

While varying the buoyancy frequency and wave velocity, some relationships were held constant (Table 2), using values from Winters (2015). The slope of internal wave propagation is given by,

$$\tan\theta = \sqrt{\frac{\sigma^2 - f^2}{N^2 - \sigma^2}}. \tag{3}$$

For the main set of simulations, a criticality of $\gamma = \tan\alpha/\tan\theta = 1.9$ is used, but results are tested and found to be qualitatively insensitive to the chosen ratio of $\tan\alpha/\tan\theta$ for another supercritical and also a subcritical value. The ratio $\sigma/f = 2.2$ is held constant for the simulations in the main parameter space of Table 1, while the additional cases of subcritical and supercritical wave reflection are tested by varying the ratio σ/f, but holding N/f constant, as shown in Table 3. All parameter values varying σ and γ still follow the relationships found for the supercritical results with $\sigma/f = 2.2$.

3. Results

a. Physical mechanism and scaling of breaking internal waves

Fig. 2 shows snapshots from the first breaking event above a supercritical slope ($\tan\alpha/\tan\theta = 1.9$), with amplitude, $V_0 = 0.25\ \mathrm{ms}^{-1}$, and stratification, $N_0^2 = 1.23\times10^{-5}\ \mathrm{s}^{-1}$. The simulation is started from rest, except for the incoming forced wave. Initially, the internal wave advects isopycnals along the slope. During the second wave period ($t = 2\ T_\sigma$) a bore of denser water is formed and advected up the slope. Halfway through this upslope phase, the water closest to the slope in the lower 20 meters begins to advect back down the slope. Convective instability near the boundary during the wave phase transition results in small overturns, with downslope flow carrying lighter

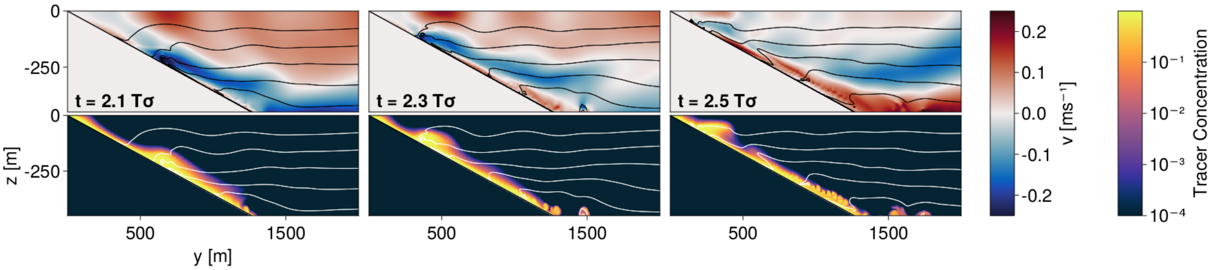

FIG. 2. Snapshots of velocity (v, top row) and dye concentration (bottom row) during the second wave period. The right column, $t = 2.5\,T_\sigma$, shows the initial small overturns found along the slope during this quasi-spin-up period. Isopycnals are marked as contour lines in all images. Animations can be found of these fields in the supporting information.

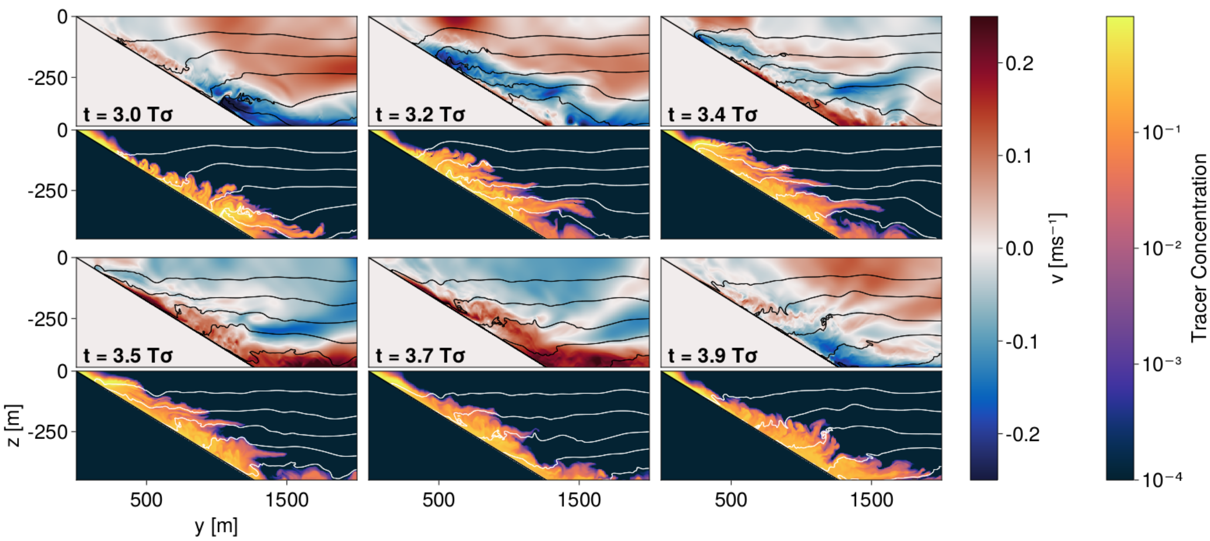

FIG. 3. Snapshots of velocity (v, first rows) and dye concentration (secondary rows) during the third wave period. The upper left plots, $t = 3.0T_\sigma$, show the initial large upslope bore (blue), consistently seen in all following wave periods. Isopycnals are marked as contour lines in all images. Animations can be found of these fields in the supporting information.

water near the boundary while the upslope phase still carries denser water aloft, as seen in Fig. 2 (right column). These initial overturns are similar to those described in low amplitude velocity cases (Drake et al. 2020; Kaiser et al. 2022), but this phasing is here only characteristic of those initial few wave periods and is not the focus of this work.

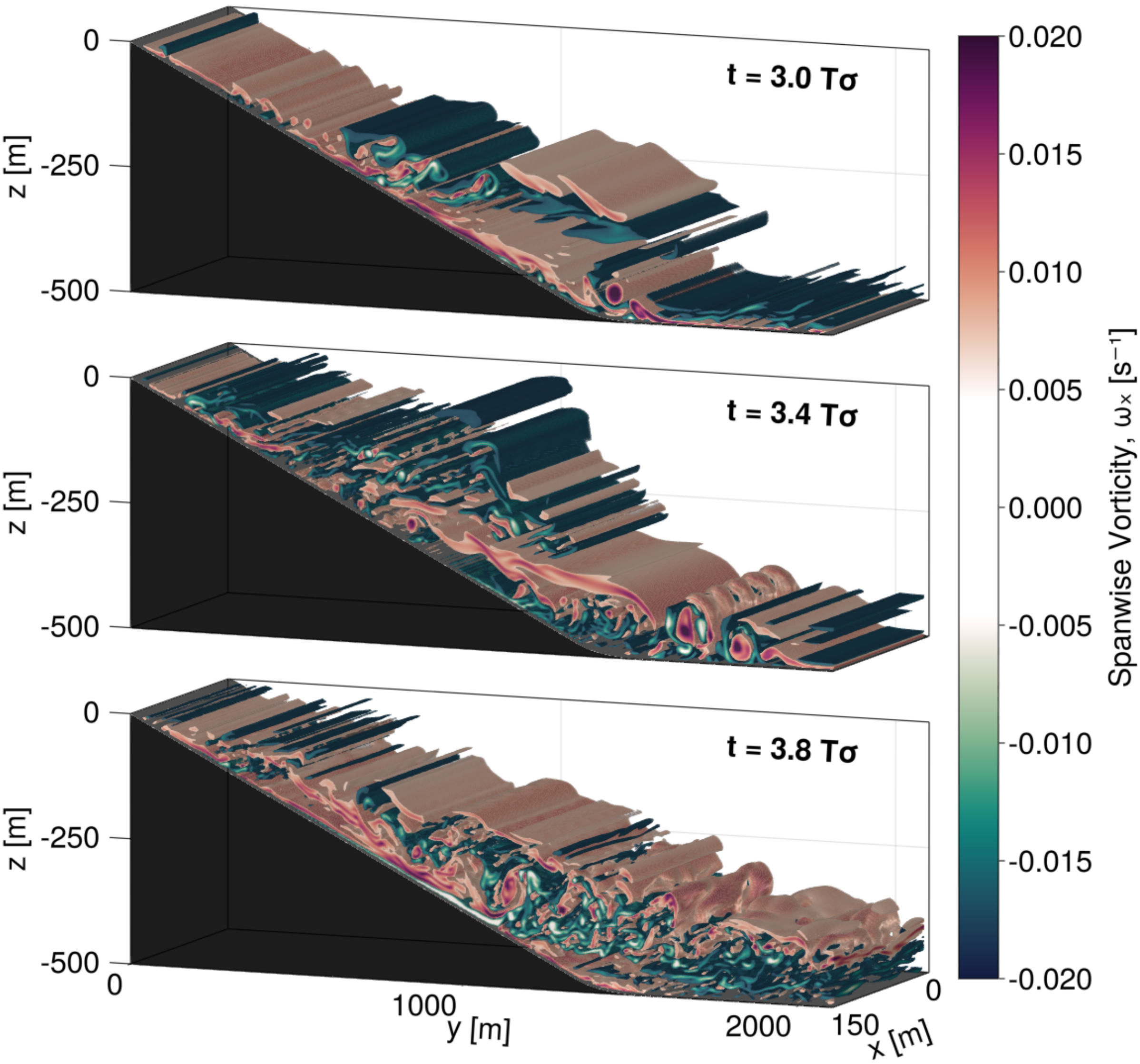

FIG. 4. 3D contours of the spanwise (ω_x) component of the vorticity for the same simulation in Fig. 3. Values shown at three points within the wave period show indicate the development of 3D structures and the transition to turbulence in the third wave period. An animated version of this figure is available in the supplementary material.

Fig. 3 depicts the characteristic overturning process following these initial small breaking events for the same simulation as Fig. 2, representative of the evolution seen across the surveyed parameter space. At the beginning of the upslope phase, a much larger bore of dense water immediately overturns and breaks along the slope around 300 m depth. This is followed by smaller overturns at the transition to downslope flow, similar to those discussed in the earliest wave periods, however, these are not as significant as the second overturn event which occurs when downslope flow is at a maximum, bringing lighter water under heavier water, as seen at $t = 3.5T_\sigma$ in Fig. 3. Similar downslope overturns observed in the Kaena Ridge, and in LES have been attributed to shear instability (Aucan et al. 2006; Gayen and Sarkar 2011). The bore leading a sharp transition to upslope flow, and the intensified flow near the boundary during the downslope phase, often accompanied by an increase in turbulence and mixing, have been found in both numerical simulations and observations of tidal flow over steep topography (Cyr and van Haren 2016; Aucan et al. 2006; Winters 2015; Slinn and Riley 1998). As the transition to upslope flow is particularly rapid, the upslope bore often directly interacts with the downslope overturns in these simulations. These competing velocities can create multi-layered gravitational instabilities resulting in even larger overturns and more mixing. The spanwise vorticity for the same simulation shows the transition to three-dimensional turbulence during this wave period (Fig. 4). Along-slope vortices develop, with across-slope variations at the transition between up and downslope flow ($t = 3.4T_\sigma$). The downslope breaking event causes an increase in turbulence, with smaller-scale structures appearing, and more regions of high vorticity developing along the slope. This process continues with two overturning and mixing events during each wave period, though following wave periods start with pre-existing three-dimensional structures instead of the two-dimensional overturning features seen at $t = 3.0T_\sigma$ in Fig. 4.

A survey of simulations with velocities ranging from $V_0 = 0.05$ to 0.55 ms^{-1} and stratifications between $N_0^2 = 2.56 \times 10^{-6}$ and 3.6×10^{-4} s^{-1}, show the bores, overturns, and, consequently, breaking events along the slope all follow similar patterns as described above. However, a small set of simulations run with subcritical slopes, small values of velocity, $V_0 = 0.05$ ms^{-1}, or strong initial stratification, $N_0^2 = 3.6 \times 10^{-4}$ s^{-1}, did not always show these same general characteristics and breaking events, as topographic interactions remain linear and stably stratified (Klymak et al. 2012; Balmforth and Young 2002). Smaller velocities or stronger stratification could not be tested, since the grid resolution would not be able to capture the necessary turbulent scales in these cases.

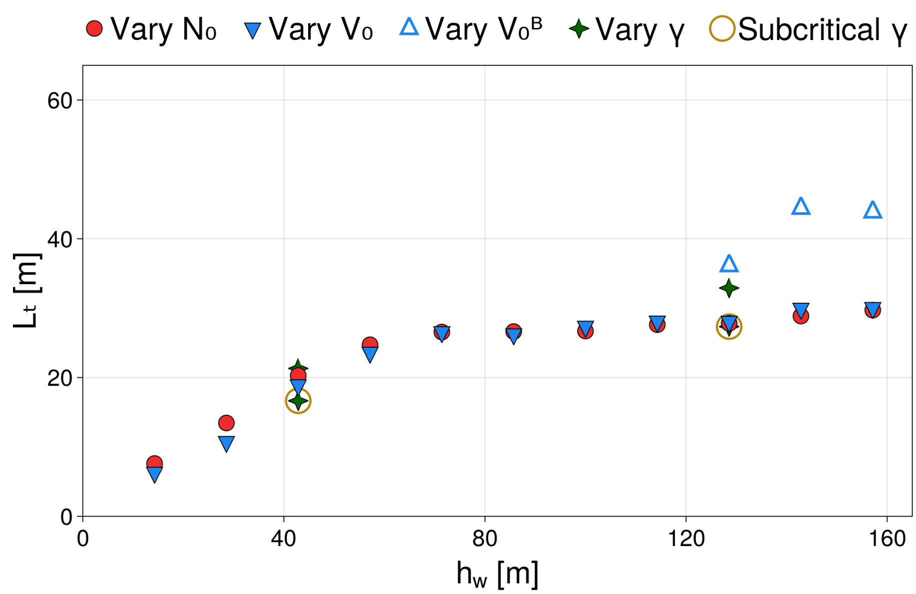

FIG. 5. RMS Thorpe Scale, L_t, for each simulation is compared to h_w, showing an approximately linear relationship between the two. Simulations varying the slope criticality, γ, hold N constant for two V_0 values, shown by the green stars. A similar relationship is also found for subcritical cases (gold rings) where σ is varied. Simulations with the largest expected overturns have some dependence on numerical domain size, as seen in the V_0^B simulations where extra vertical space above the slope was included.

We focus analysis in particular on the importance of what we term the *effective wave height*,

$$h_w = \frac{V_0}{N_0}, \tag{4}$$

where again V_0 is the wave velocity amplitude and N_0 is the interior buoyancy frequency (note that this parameter was denoted δ in Winters 2015). This height scale is analogous to h_{eff} but scales with the wave velocity itself rather than with the steady interior flow velocity. It can thus be interpreted physically as the largest vertical distance a water parcel can be moved before losing all of its wave kinetic energy to potential energy (Winters 2015; Winters and Armi 2013). Below we show the effective wave height parameter organizes many of the simulation results across a wide-range of V_0 and N_0 values, spanning h_w values from 14.3 to 157.1 m (Table 1).

The effective wave height is expected to set an upper bound on the wave overturn size. Overturns can be measured with the Thorpe scale (Thorpe 1977), defined as the root mean square (RMS) of the displacement necessary to adiabatically reorder the buoyancy profile to make it gravitationally stable. Overturns estimated from the simulations were only counted if the buoyancy range within the overturn exceeded a threshold of $\Delta b > 2\,\Delta z\, N_0^2$ and the length scale $L_t > 2\Delta z$ to avoid spurious identification of overturns not resolved by the numerical grid. Fig. 5 indicates this relationship between the effective wave height and the resulting Thorpe average for each simulation, L_t. There is an approximately linear relationship between h_w and L_t, suggesting that the simple measure of the effective wave height effectively scales the breaking events near the boundary. The small differences in overturn size for large h_w simulations, could be a domain dependence on the calculation of Thorpe scale as h_w approaches 100 m. A set of simulations, V_0^B, where the vertical domain is increased by 150 m results in an increase in the measured L_t. The plateau in these averaged results also heavily samples an increasing number of small overturns present alongside the larger overturn events discussed earlier. Therefore, the effective wave height could still be controlling the size of the largest parcel displacements, and thereby the most energetic overturns, while the RMS estimate of Thorpe scale remains smaller.

b. Overturns and dissipation in breaking waves scaled by h_w

Instead of directly measuring the turbulent dissipation rate, ϵ, the average dissipation rate is often estimated from the size of the overturns in a stratified column (Dillon 1982; Thorpe 1977). The Ozmidov scale, L_o (Hopfinger 1987), gives the size of the largest eddy that is not dampened by buoyancy (McPhee-Shaw and Kunze 2002; Jalali et al. 2017), and is directly related to the dissipation rate by,

$$L_o^2 = \epsilon / N^3 \tag{5}$$

Assuming a near-constant Richardson number, the Thorpe and Ozmidov scales are linearly related by, $L_0 = C L_T$, where C is a dimensionless constant of order 1 (Lu et al. 2021; Dillon 1982). Then, the turbulent dissipation rate can be estimated as $\epsilon \approx C^2 L_T^2 N^3$. The often-used constant value $C = 0.8$ (Dillon 1982), results in the relationship $\epsilon \approx 0.64 L_T^2 N^3$. This connection between Thorpe scale and dissipation rate has been taken advantage of in observations, where overturns can be quantified in profile data (Cyr and van Haren 2016). The relationship between dissipation rate

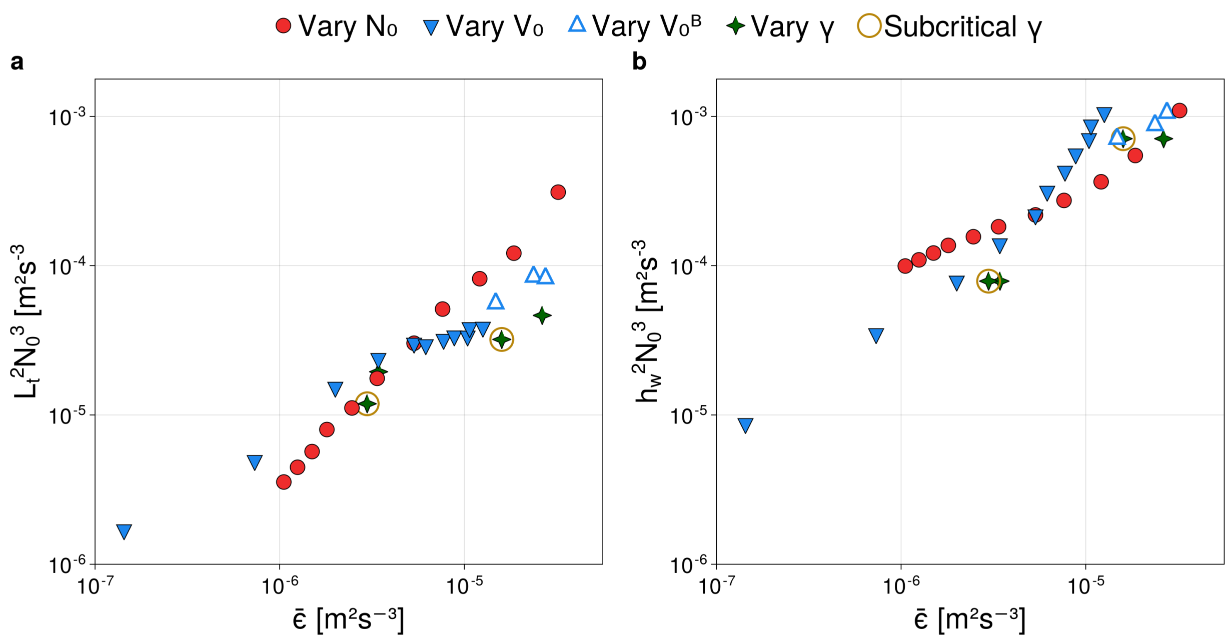

FIG. 6. The average dissipation, over waves 6-10, is compared to Thorpe Scale (a) and h_w (b). Results are shown for simulations that vary V_0 (solid blue markers), holding $N_0 = 3.5 \times 10^{-}3$, and vary N (solid red markers), holding $V_0 = 0.25$ ms^{-1}. Simulations varying slope criticality (solid green markers) and increased domain size (open blue markers) also show a similar relationship.

and estimates based on Thorpe scaling is shown in Fig. 6a for varying simulations, where $\bar{\epsilon}$ is the average dissipation, calculated directly and averaged over wave periods 6 through 11, and N is determined by the initial buoyancy frequency, N_0. The Thorpe-scaled dissipation rate estimate reasonably approximates the true dissipation rate across more than two orders of magnitude, although there is some additional parameter dependence not captured in this scaling. Simulations with varying buoyancy frequency (*Vary* N_0) show an approximately linear relationship, whereas simulations with varying velocity (*Vary* V_0) have a generally shallower slope with a flattening at higher dissipation rates. This flattening is less pronounced for simulations with additional vertical domain size (*Vary* V_0^B), suggesting (as above), some dependence on the computational domain for the largest wave velocities ($V_0 > 0.4$ ms^{-1}).

A similar scaling for the dissipation rate can be formed using h_w as the relevant vertical scale (Fig. 6b),

$$\epsilon \approx C' h_w^2 N_0^3, \tag{6}$$

where, for the simulations here, we find a best-fit coefficient of $C' \approx 0.02$. In these simulations, h_w captures the impact of both changes in the wave velocity and initial buoyancy frequency on breaking events, including for the simulations with different slope criticality. Simulations with varying V_0 have a steeper slope at higher dissipation rates than that of the more linear relationship found in the N_0 varying simulations. Increasing the vertical domain size reduces the steepness in the velocity-varying results, indicating the same dependence on the domain as Fig. 6a. Using the effective wave height reasonably reproduces the simulated bulk dissipation rates, despite relying only on the interior stratification and wave velocity, suggesting its potential utility in observational analyses (as discussed further in section 4)

c. Boundary layer and interior exchange through adiabatic pumping

The presence of turbulence and overturns near sloping boundaries alone does not mean breaking internal waves necessarily generate efficient mixing. To maintain efficient mixing along sloping boundaries, there needs to be a pathway for the restratification of the BBL. The breaking of internal waves on the downslope phase creates well-mixed boundary waters right before the upslope phase begins, over a vertical scale limited by effective wave height, h_w. The incoming dense bore is led by a region of strong buoyancy gradients, visible in the collapsed isopycnals in Fig. 7. The presence of the strong downslope velocity from the previous overturn phase, coupled with the incoming dense bore, causes an ejection of the newly mixed boundary waters along the isopycnals into the interior. These intrusions can be seen in Fig. 7, through the slope-initialized dye and regions of increased dissipation of kinetic energy rate being expelled at $t = 5.1\ T_\sigma$. Fig. 8 shows three-dimensional snapshots after the tracer has been ejected into the interior (for a simulation with $h_w = 100$ m, the reader is referred to animations in the supporting information to help build further physical intuition). Over the course of a wave period, the tracer is pumped back and forth from the boundary, as indicated by the tendrils extending into and retracting from the interior. Such ejections and layers of increased turbulence or organic materials are often seen in numerical simulations, lab experiments, and observations (Cyr and van Haren 2016; McPhee-Shaw 2006;

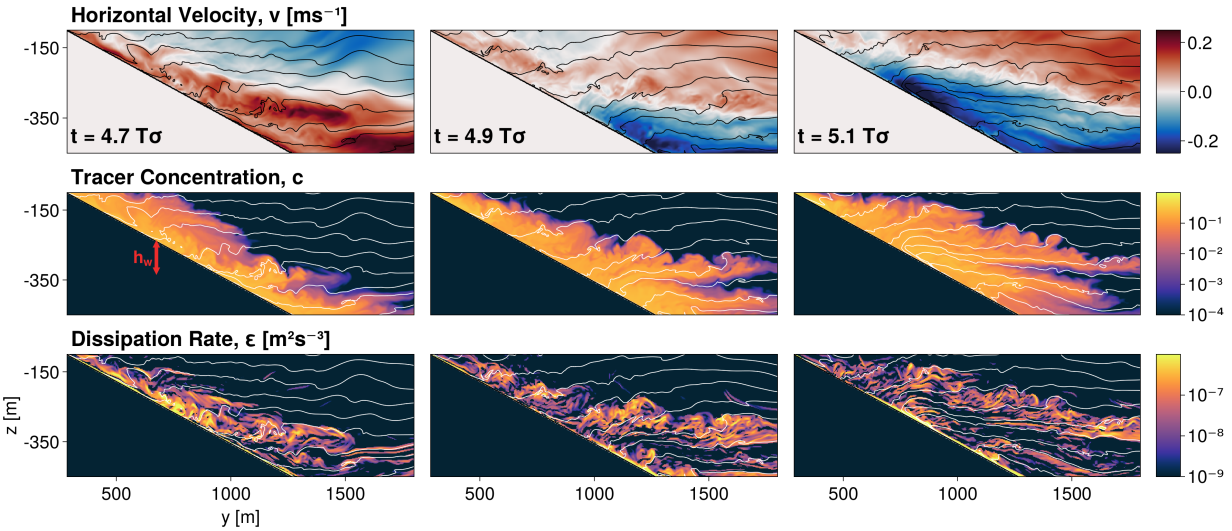

FIG. 7. Horizontal velocity, slope initialized tracer, and dissipation of kinetic energy rate during an ejection event. Isopycnals in intervals of $\Delta b = 5 \times 10^{-4}$ marked in all images. At the end of the downslope breaking event at wave period 4.7, the water is mixed within one h_w of the slope (marked in red). The isopycnals collapse on each other at the head of the incoming, upslope bore shown at wave periods 4.9 and 5.1. The tracer is ejected into the interior with tendril thicknesses close to h_w (section 3c).

Edge et al. 2021; Nokes and Ivey 1989; Winters 2015; van Haren 2023; Wynne-Cattanach et al. 2023; McPhee-Shaw et al. 2021).

The timing of the exchange process can also be seen by looking at phase-averaged Hovmöller plots of the near boundary region in buoyancy space. Each buoyancy class represents a region, $R(b,t)$ of size $\Delta b = 20\ N_0^2$ within $1.1\,h_w$ of the sloping topography, creating 25 initially equal volumes. The diagram in Fig. 9 indicates such a region shaded in blue. Fig. 10 takes the phase average over waves 4 through 10 of a representative simulation. The first row shows the average horizontal velocity (a), dissipation of kinetic energy rate (b), and stratification anomaly (c) in each buoyancy class during a wave period. The upslope phase replenishes the boundary with strong stratification, while the downslope phase has increased dissipation and weak stratification, directly before the ejection. This phasing difference, with dissipation rate and stratification inversely varying, has also been seen in simulations of barotropic tides (Ruan and Ferrari 2023; Gayen and

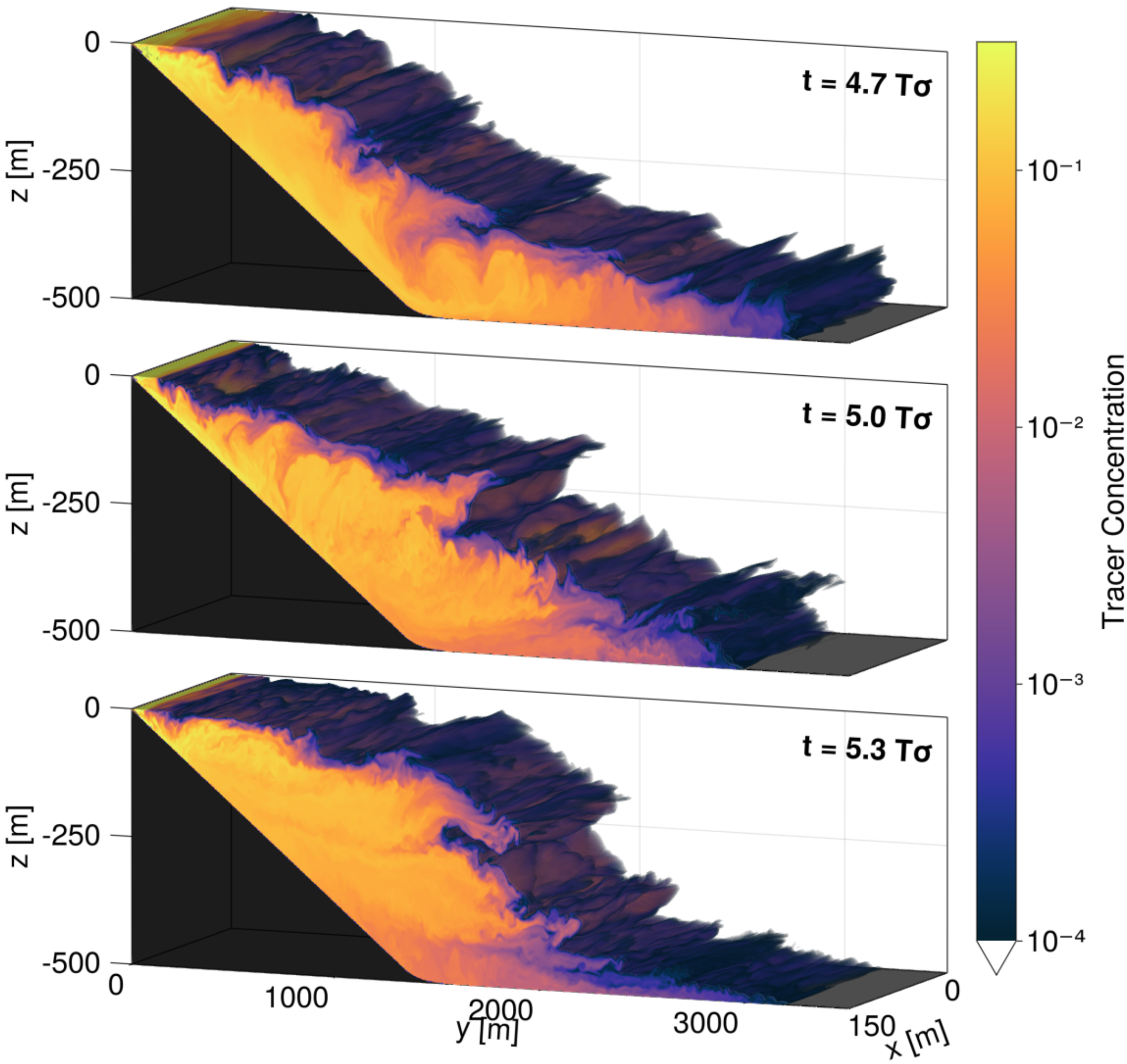

FIG. 8. 3D contours of slope initialized passive tracer concentration (log scale) for simulation with $V_0 = 0.35$ ms^{-1}, $N_0 = 3.5 \times 10^{-3}$ s^{-1}, and $h_w = 100.00$ m. Concentrations less than 10^{-4} are omitted. Values are shown at three points across the 4th and 5th wave period. Tracer is laterally ejected, extending 2500 m into the interior at $t = 5.0T_\sigma$, the transition between up and downslope flow. A 3D animation can be found of this ejection process in the supporting information.

Sarkar 2011) as well as in observations (Cyr and van Haren 2016; Nielson and Henderson 2022; Aucan et al. 2006).

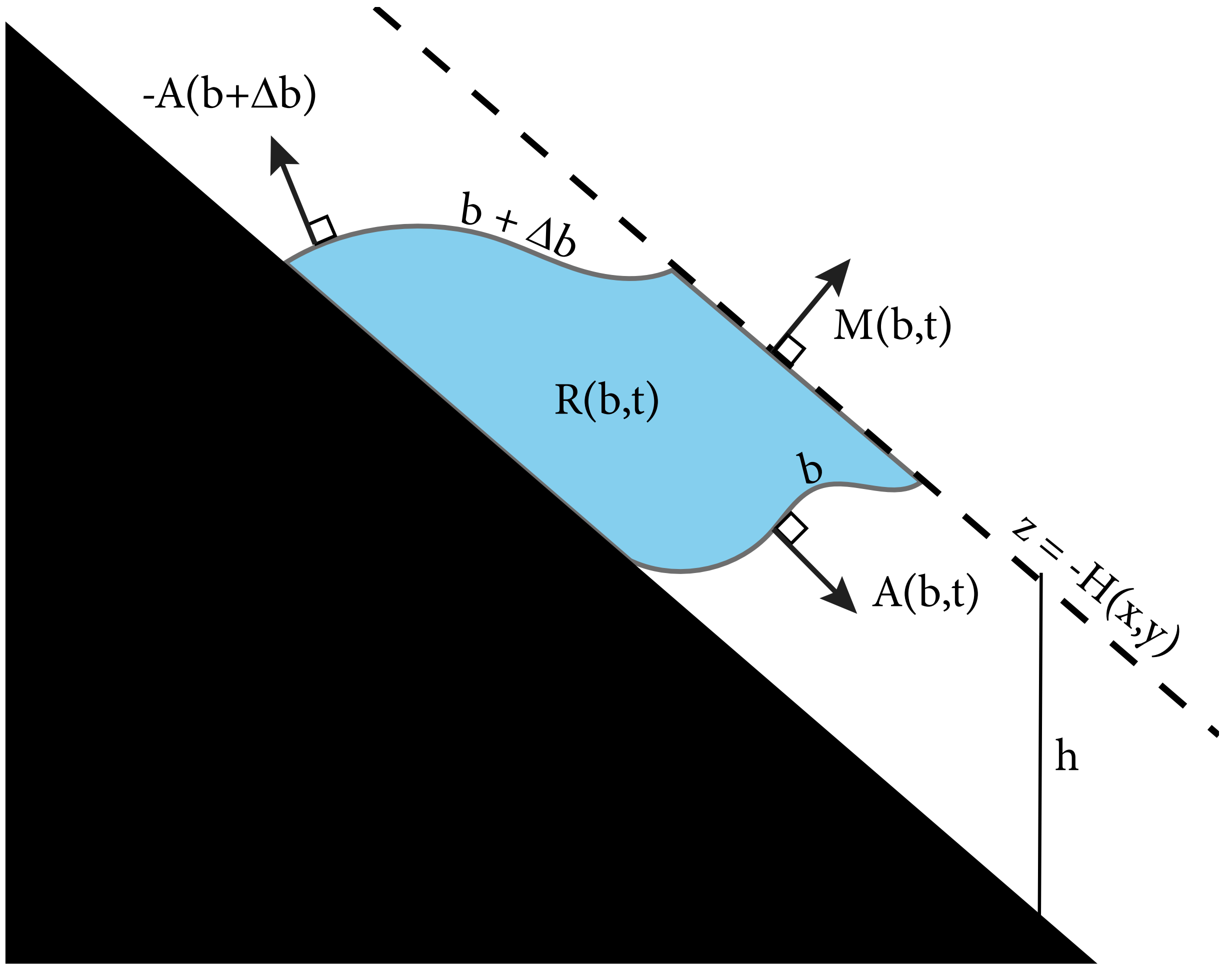

FIG. 9. Shaded volume bounded by two isopycnals, the topography, and the fixed surface $H(x,y)$. $H(x,y)$ is a vertical distance of $h = 1.1h_w$ from the slope. The diapycnal volume flux through the isopycnal surfaces is A and the flux through H into the interior is M (Marshall et al. 1999).

The near boundary volume of a specific buoyancy class will only be altered by the diapycnal fluxes through the isopycnal surfaces bounding the class, $A(b+\Delta b) - A(b)$, and volume fluxes into the interior, $M(b)$ (Marshall et al. 1999). The volume budget of a buoyancy class, $R(b,t)$, bounded by b and $b+\Delta b$, is given by,

$$\frac{\partial V(b,t)}{\partial t} = A(b+\Delta b,t) - A(b,t) - M(b,t). \tag{7}$$

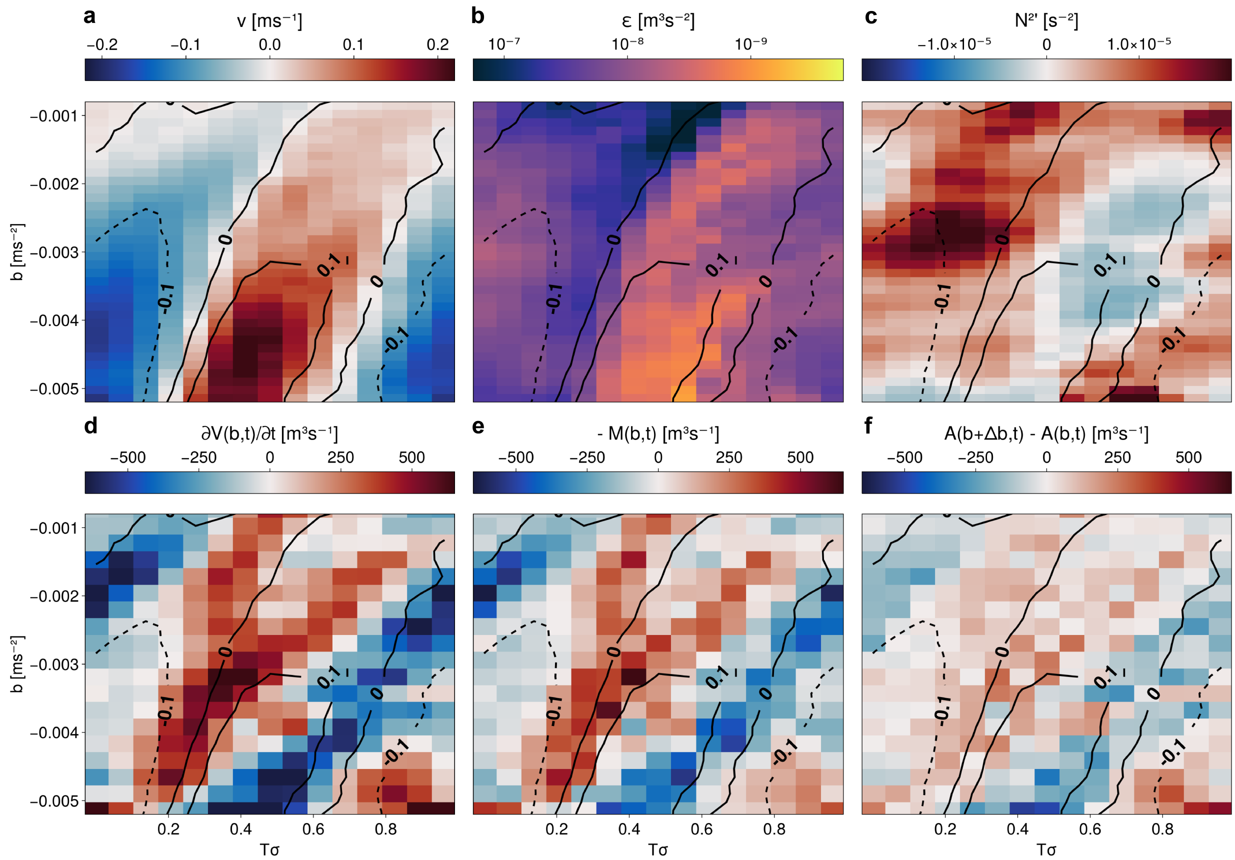

Fig. 10. Representative simulation with $V_0 = 0.35$ ms^{-1}, $N_0 = 3.5 \times 10^{-3}$ s^{-1}, and $h_w = 100.00$ m. Row one shows the average (a) horizontal velocity, (b) dissipation of kinetic energy rate, and (c) stratification anomaly in each buoyancy bin. Row two is the buoyancy binned volume budget within $1.1h_w$ of the slope (refer to Fig 9 and Eq. 7): (d) the buoyancy class volume rate of change, (e) the flux of volume from the interior, (f) the flux through the isopycnal surfaces, calculated as the residual of (e) and (f). All are phase averaged over waves 4 - 10. Contours show the average horizontal velocity in each buoyancy class, indicating the ejections into the interior occur at the transition between up ($v < 0$) and downslope flow ($v > 0$). Dissipation rate is strongest, while stratification is weakest, during the downslope phase.

Fig. 10 compares these terms, where positive values indicate an increase in boundary volume. The contraction and dilation of the near boundary buoyancy classes occur at the transitions between wave phase, (along the $v = 0$ ms^{-1} contours). These changes in near-boundary volume are largely balanced by the volume fluxes into and out of the interior. At the transition between downslope ($v > 0$) and upslope ($v > 0$) flow the loss of volume near the boundary is accompanied by a flux

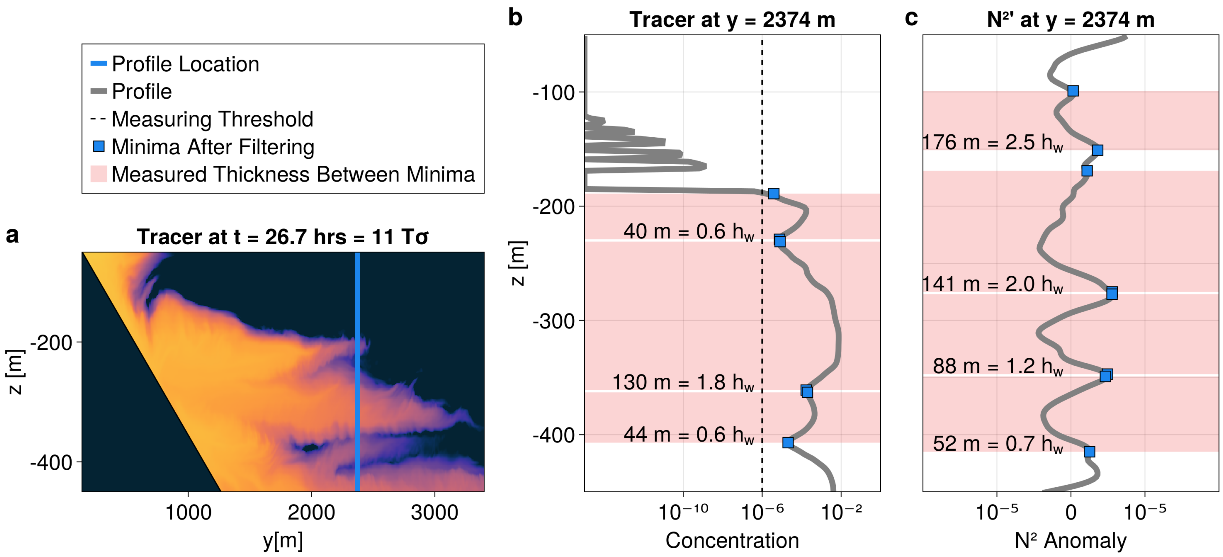

FIG. 11. Depiction of intrusion thickness in a representative profile. (a) tracer concentration at $t = 11T_\sigma$, after the initial smoothing, discussed in Appendix A. (b) the vertical profile of the tracer concentration taken at the location marked by the blue line in (a). The dashed line indicates the threshold for allowable values of concentration used in the calculation. (c) the vertical profile of stratification anomalies at the same location. Red shaded regions indicate an included intrusion calculation for either measure, with blue markers at the endpoints. These measured thicknesses in (b) and (c) are averaged in both time and space to find a single average thickness of tracer intrusions, L_{tr}, and stratification anomalies, L_{N^2} for each simulation.

of volume into the interior ($-M(b,t) < 0$), indicating an adiabatic pumping process, creating the exchange between the boundary and interior. While most of the change in volume close to the slope is due to adiabatic motions, the residual between the $\partial V/\partial t$ and $-M$ is not negligible, indicating there are also irreversible changes due to diapycnal volume flux through isopycnal surfaces, $A(b+\Delta b) - A(b)$ during the exchange process, to be discussed more in section 3d.

The exchange of fluid between the boundary layer and interior can be quantified using the passive tracer initialized along the slope (eg. Fig. 1). The along isopycnal ejections take the form of tendrils of high concentration extending into the interior (Figs. 7, 8), from which an average tracer intrusion thickness, L_{tr}, can be calculated. Details of the method are given in Appendix A, however, Fig. 11a,b shows an example of the tracer concentration thicknesses calculated from a single profile for a representative time step and horizontal location. The thickness of these layers in the interior

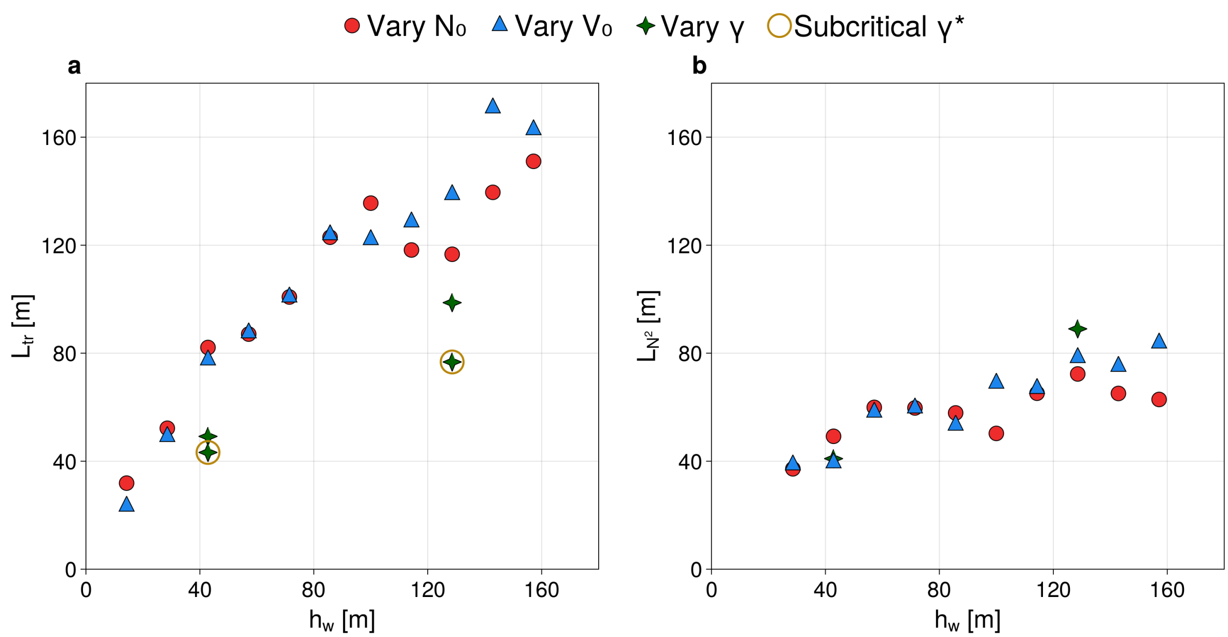

FIG. 12. Comparing h_w to the thickness of the dye intrusions away from the slope (a) and the thickness of the patches of stratification anomaly (b). This shows a linear relationship of order 1, holds over simulations that vary V_0 and N_0, as well as varying ratio of f/σ, for two V_0, h_w values, changing the criticality to compensate. Plots show the relationship still holds where σ results in a subcritical slope relationship, indicated by gold rings. Subcritical simulations are not shown in panel b, as linear wave dynamics obscured well-mixed regions using this method (Appendix B)

scales 1-1 with, h_w, as shown in Fig. 12a, indicating that the constraint on overturning size along the boundary is reflected in the range of density classes over which the boundary layer-interior exchange occurs.

An alternate signature of exchange between the boundary layer and interior is stratification anomalies resulting from the along-isopycnal transport of mixed water from the boundary. In a well-mixed intrusion, the buoyancy anomaly, relative to the initial condition, will be positive in the lower half of the intrusion and negative in the upper half, with related stratification anomalies (Fig. 11c, with details of the calculation given in Appendix B). Fig. 12b indicates that the stratification anomaly thickness, L_{N^2}, also scales linearly with effective wave height when averaged over several wave periods for each simulation. The organization of the stratification anomaly with h_w emphasizes the importance of diabatic processes in wave breaking and subsequent ejection.

These results indicate that water mixed along the lower boundary, with overturn size scaled by h_w, is ejected into the interior along isopycnals, setting the magnitude of this interior exchange and connecting the intrusion thickness to the along-boundary mixing.

d. Turbulent buoyancy fluxes

The ejection of mixed water from the boundary into the interior provides a pathway for maintaining efficient mixing, hence here we consider the associated water-mass transformation, as described by the divergence of diapycnal buoyancy fluxes. Due to the nonlinear nature of the internal waves, it is convenient to decompose the perturbations into periodic wave and turbulent motions such that, (Reynolds and Hussain 1972)

$$b = \bar{b} + \tilde{b} + b'. \tag{8}$$

Here, $\bar{b}$ is the mean buoyancy field, where $\overline{(\cdot)}$ indicates temporal averaging over several wave periods, $\tilde{b}$ is the periodic portion of the buoyancy field found using the phase average, $\langle\cdot\rangle$,

$$\langle b \rangle = \bar{b} + \tilde{b}, \tag{9}$$

and b', as the residual, represents the turbulent motion. This triple decomposition using only temporal averaging results in the following equation for the evolution of the mean buoyancy,

$$\frac{\partial \bar{b}}{\partial t} + \bar{\mathbf{u}} \cdot \nabla \bar{b} = -\nabla \cdot \overline{(\tilde{\mathbf{u}}\tilde{b})} - \nabla \cdot \overline{(\mathbf{u}'b')} + \overline{\nabla \cdot \kappa \nabla b}. \tag{10}$$

Fig. 13 shows the flux divergences from the right-hand side of (10). The non-linear wave term dominates over the turbulent term, though there is little difference between the two in sign throughout the near-slope domain. Directly above the topography, there is a thin layer, ~ 20 m thickness, where the vertical flux convergence is positive. Similar has been speculated to be important for upwelling in the abyssal circulation, however critically here we note that this region of vertical flux convergence is entirely offset by the *horizontal* flux divergence. Further from the topography, the vertical flux convergence is negative, but partially offset by positive horizontal flux convergence. These results indicate the total buoyancy flux is divergent near the boundary, with convergence in the interior above the wave-breaking region. The effective wave height shown to

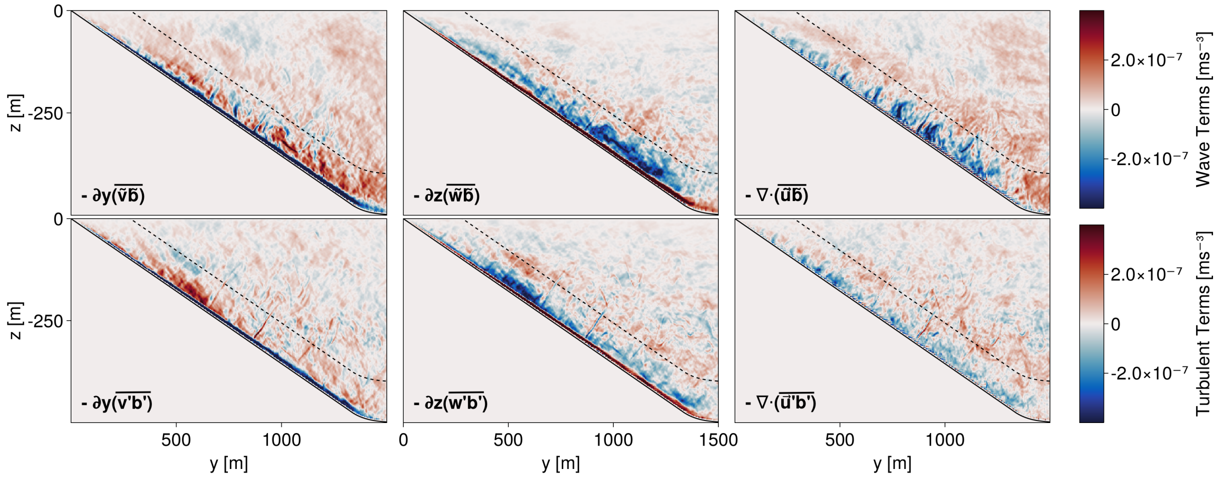

FIG. 13. Wave-averaged buoyancy fluxes indicate the similar magnitude importance of the horizontal and vertical buoyancy fluxes to mixing along the slope, as well as a relationship between the mixed region and effective wave height, h_w, where the dashed line is one h_w above the slope. The nonlinear wave effects dominate the buoyancy evolution over the turbulent term. Both flux terms show near-boundary buoyancy flux divergence.

scale the breaking and exchanges also scales the height above boundary where the buoyancy flux divergence occurs (dashed line in Fig. 13).

The vertical buoyancy flux is often assumed to be the dominating component in boundary mixing (Garrett et al. 1993), but these numerical results suggest both horizontal and vertical components play a significant role due to the order-1 aspect ratio of overturns and the development of horizontal buoyancy gradients during the wave breaking events (Fig. 3). Buoyancy flux plots of 2D tidal simulations by Ruan and Ferrari (2023) also show horizontal and vertical fluxes of similar magnitude, though the relatively large ratio of h_w to grid-spacing in their simulations may have resulted in under-resolved wave-breaking overturns. The order one aspect ratio in horizontal and vertical flux variations indicate the horizontal buoyancy flux divergence cannot be neglected in these simulations (cf., Holmes and McDougall 2020). By considering both components, the near-boundary buoyancy flux convergence is canceled out entirely, and the remaining divergence within the overturning region is less than that of the vertical component alone.

The total buoyancy flux convergence in (10) is primarily balanced by mean buoyancy advection, such that $\partial\overline{b}/\partial t \approx 0$ (Fig. 14). This implies a mean downwelling along the topography, again emphasizing the role of the horizontal buoyancy flux in canceling the thin layer of vertical buoyancy

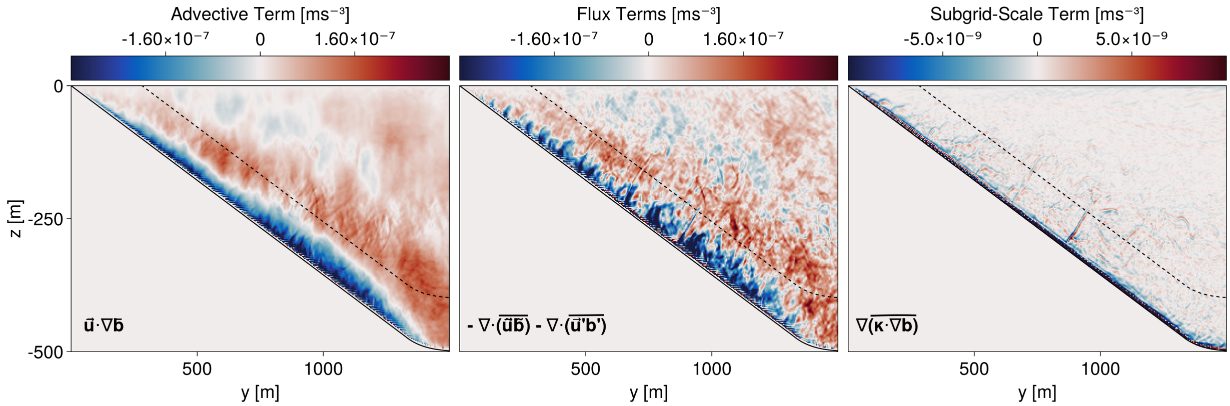

FIG. 14. Agreement between the wave-averaged advective term and the buoyancy fluxes indicate this implied near-bottom downwelling is necessary to balance advection in a steady state solution. The subgrid-scale term is two orders of magnitude smaller than the others.

flux convergence near the bottom. However, it is important to note that the mean buoyancy does not reach a steady state during these simulations. Fig. 15a shows wave-averaged buoyancy (gray contours), compared to the initial condition with uniform stratification (black contours). The water at the top of the slope is getting denser, while water at the the bottom of the slope gets lighter, indicating a convergence of mass into intermediate buoyancy classes. This signature continues to intensify throughout these simulations. Compared to the relative uniformity along the slope of the buoyancy flux divergence in Fig. 14, the total change in wave-averaged buoyancy is much more dependent on the location of the initial buoyancy class along the slope.

The residual in the buoyancy-binned volume budget (Fig. 10f) also indicates a phase-dependent diapycnal volume flux through the isopycnal surfaces, $A(b+\Delta b) - A(b)$. Diapycnal fluxes into near-boundary buoyancy classes occur near the transition from upslope to downslope flow. While the breaking is strongest during the downslope phase, the stratification is also weakest during this phase, allowing for a difference in phase between the strongest diapycnal fluxes and the peak of the breaking event (Fig. 10b,c). Fig. 15c shows the same near-boundary volume budget wave-averaged over the same wave periods. There is an overall gain of volume in the near boundary region through isopycnal surfaces around $b = -0.003$ and -0.004 ms^{-2}. This volume change is not as large as that of the interior-exterior transport, as that is largely balanced by reversible changes in near-boundary volume. Extending the binned region out to $5h_w$ (the thick black line in Fig. 15a), the total change

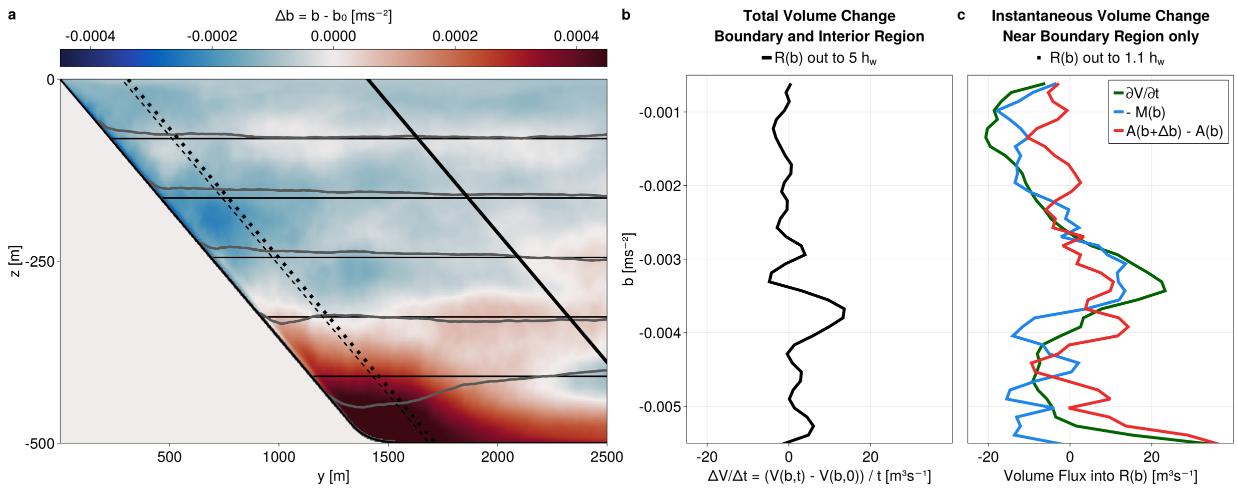

FIG. 15. (a) shows the change in wave-averaged buoyancy, $\bar{b}$, (gray contours) compared to the initial condition, b_0, (black contours). Contours represent isopycnals at 10^{-3} ms^{-2} intervals, and the thin dashed line is $1\,h_w$ from the slope. The wave-averaged buoyancy is not in steady state throughout the simulation, with buoyancy decreasing at the top and increasing at the bottom. Plot (b) shows the integrated volume change in buoyancy space from (a), normalized by the change in time, where H is marked in (a) as the thick solid line, $5\,h_w$ from the slope. There is an increase in volume into an intermediate buoyancy class around $b = -0.004$ ms^{-2}. Plot (c) shows the instantaneous volume budget from (7) over a region extending $1.1h_w$ from the slope, indicating the total volume change out to $5\,h_w$ in (b) is most likely due to a diapycnal buoyancy flux in the near-boundary overturning region. All plots are wave-averaged over the same range as the phase averages in Fig. 10, waves 4 - 10.

in volume ΔV, normalized by the difference of time, indicates a convergence of mass into a similar buoyancy class, shown in Fig. 15b. By including interior waters, the volume changes ignore the impact of along-isopycnal motions close to the boundary, focusing on the irreversible volume fluxes. These increases culminate in a buoyancy class that is 90% larger than it was initially. In physical space, this buoyancy class is also near the transition between densening and lightening regions in Fig. 15a.

These results can be synthesized as follows. During the breaking events boundary fluid is mixed on time scales much smaller than a wave period, with brief moments of intense mixing and interior exchange in response to the strong downslope flow and the upslope dense bore (Fig. 10). The timing of water-mass transformation during the wave breaking is not necessarily coincident with the strongest kinetic energy dissipation rates, as stratification and turbulence covary (Fig. 10f and Cyr and van Haren 2016). In the time-mean, this leads to a pattern of buoyancy flux divergence within $\sim 1\,h_w$ of the boundary, with horizontal flux divergences playing a significant role in the total (Figs. 13, 14). This flux divergence is largely balanced by mean downslope advection (Fig. 14), however, the simulations are not in steady state, such that there is an ongoing convergence of mass into intermediate density classes (Fig. 15). Determining to what extent these results depend on our numerical configuration (both domain size and treatment as an initial value problem), and what selects the convergent buoyancy class more generally in realistic settings is beyond the scope of the present work. However, the results presented here offer guidance towards interpreting observations, particularly highlighting the role of lateral fluxes, the dependence of diapycnal volume fluxes on along-slope position, and the subsequent ejection of mixed waters into the interior along-isopycnals.

4. Conclusion

Three-dimensional LES were used to demonstrate the connection between breaking internal waves on sloping topography, overturn size, and along-isopycnal intrusions. The simulations indicate there are two main wave breaking points within the wave period. The internal wave overturns and breaks when the downslope velocity is strongest, and is followed by the rapid appearance of a dense, upslope bore and the next overturn event (Fig. 3). Such overturns are often seen in observations and other numerical simulations (Aucan et al. 2006; Cyr and van Haren 2016; Winters 2015; van Haren and Gostiaux 2012a; Gayen and Sarkar 2011). Our results suggest the effective wave height, h_w, defined as the ratio of wave velocity to background buoyancy frequency (4), governs the scale of the overturns found along the slope as well as the resulting dissipation rate of kinetic energy (Figs. 5, 6).

After mixing boundary waters, the strong stratification at the head of the upslope bore forces the mixed fluid into the interior. Fig. 10 shows this lateral pumping with ejections into the interior between the most energetic breaking downslope phase and the strongly stratified upslope phase. The effect of the near-boundary wave breaking is communicated into the interior through these along-isopycnal intrusions, with tracer intrusion thicknesses again scaled by the effective wave height, h_w (Fig. 12a and see Winters 2015). During a breaking event, fluid is mixed over a near-boundary layer approximately 1 h_w thick and is subsequently ejected into the interior, resulting in stratification anomaly thicknesses in the interior also scaled by the effective wave height (Fig 12b).

Observed estimates of dye releases and organic tracer intrusions also indicate good agreement with the findings presented here. Using the tracer thickness diagnostic method (Appendix A), measurements of dissolved oxygen anomaly as a passive tracer in the Monterrey canyon indicate an average intrusion thickness over several profiles of 105 m (McPhee-Shaw et al. 2021). The results presented here would predict an effective wave height, and corresponding intrusion thickness between 55 – 100 m, based on observed stratification and current velocity measurements in this region of the canyon (McPhee-Shaw et al. 2021; Kunze et al. 2012; Petruncio et al. 1997). Observations using a cross-canyon mooring array during a dye release in the Rockall Trough as part of the Boundary Layer Turbulence (BLT) experiment indicate a h_w of about 115 m (Wynne-Cattanach et al. 2023). The measured intrusion thickness of released dye from mooring data fell around 100 – 150 m (Wynne-Cattanach et al. 2023), in good agreement with the estimated effective wave height size. With a stratification of $N^2 = 3 \times 10^{-6}$ s^{-2}, the expected average dissipation of kinetic energy rate (Fig. 6b) matches the bursts of dissipation on the order of 10^{-6} m^{2}s^{-3} seen during breaking events in the trough, as well (B. Wynne-Cattanach, personal communication, February 22, 2024). Though the simulations presented in this work were highly idealized, the simplicity of the scaling suggests it may be useful for interpreting observations, both in terms of near-boundary mixing processes and the exchange between the boundary layer and interior.

The total buoyancy flux averaged over several wave periods (Fig. 13) shows especially strong divergence within the overturning region extending a height of approximately h_w above the slope. In this region, both horizontal and vertical buoyancy fluxes contribute significantly to the total flux divergence, a consequence of the order-1 aspect ratio of overturning features along with the development of strong horizontal buoyancy gradients that precede breaking events. While this near-slope divergence is mainly balanced by mean downslope advection (Fig.14), a volume budget in buoyancy space shows there is a net diapycnal flux into some intermediate buoyancy classes along the slope, with a convergence of mass in nearby buoyancy classes as well (Fig. 15). This net diapycnal flux is driven by short bursts of intense mixing within a wave phase (Fig. 10), at the transition between the upslope and downslope phases. Covariances of turbulent dissipation and stratification anomalies, along with the role of lateral fluxes, suggest caution in the interpretation of vertical profile data or the use of time-averaged fields.

The net diapycnal buoyancy flux divergence is largely balanced by mean downslope buoyancy advection, however, in these simulations, there is also a convergence of mass in an intermediate density class, midway along the slope (eg. Fig. 15). How this result changes in the presence of a more realistic slope geometry and internal wavefield—including variations in slope criticality, bottom roughness, 3D bathymetry such as canyons, and time-varying wave forcing—is an open question with important implications for understanding the net mixing during these types of breaking events. Likewise, the Lagrangian watermass evolution, in the presence of near-boundary mixing and strong interior-boundary layer exchanges could be usefully considered in future work. Results presented here suggest that the effective wave height, h_w, provides a useful constraint on wave energetics that can be applied to understanding the near-boundary breaking zone, adiabatic exchanges of mixed-fluid with the interior, and the rate of turbulent dissipation.

Acknowledgments. The authors thank Gregory L. Wagner, Ali Ramadhan, and Gabriel Weymouth for assistance in implementing the immersed boundary method in Oceananigans (Ramadhan et al. 2020), and Tomás Chor for advice on model setup and diagnostics. This material is based upon work supported by the National Science Foundation under Grant Numbers OCE-1948953 and OCE-2232441.

Data availability statement. Model configuration and analysis scripts will be made publicly available via github.com before manuscript publication.

APPENDIX A

Numerical calculation of tracer intrusion thickness

The thickness of interior dye intrusions is calculated for each simulation. At every time step the tracer concentration, initialized as a hyperbolic tangent function along the entire slope, is averaged in x, and smoothed in y via a rolling window of 40 data points at a time. An example time step can be seen in Fig. 11a after smoothing. For each vertical profile of the tracer, the numerical derivative with respect to z is used to find all local minima in the profile. If the sign of the derivative changes from negative to positive, then the concentration has reached a minimum, indicating a possible boundary for an intrusion. The near-slope region is excluded by removing points within 6 m of the slope, to avoid including the bottom boundary layer itself in the calculation of intrusion thickness.

As can be inferred from the profile in Fig. 11b, the minima found are not always relevant. The local minima could just be a slight change in concentration within a much larger intrusion, or it could be a minima corresponding to an intrusion with very low concentration. To avoid such cases, intrusions are only included from a dye profile if the maximum concentration within a candidate intrusion reaches a threshold of 10^{-4}, and its bordering minimums dropped at least half the concentration of the maximum. Such examples can be seen marked by the blue markers in Fig. 11b. For example, if the maximum concentration of an intrusion in a certain dye profile is 10^{-3}, then the bordering minima would have to be less than 5×10^{-4} to include that intrusion in the average. The thickness of each intrusion is then measured above a 10^{-6} cutoff concentration of dye in the profile. So, even if the minimums surrounding an intrusion dropped to 0 concentration, the thickness would only measure to where the concentration had dropped to 10^{-6}.

Once bounds are identified on the intrusions, the thickness can be easily found as the difference between the two minimums. The thickness of three such intrusions is marked in Fig. 11b by the red regions. All of these accepted intrusion thicknesses were averaged in space for each time step, and then in time over the last 5 wave periods to get an average intrusion thickness for each simulation. This is the value used in Fig. 12. Various other methods and criteria for extracting intrusion thickness were also tested and the results were found to be qualitatively insensitive.

APPENDIX B

Numerical calculation of interior stratification anomaly thickness

Stratification anomalies can also be used to define the thickness of intrusions, using the instantaneous N^2 values calculated in each simulation. The stratification anomaly is defined as $N^{2\prime} = N^2 - N_0^2$. To smooth the resulting values, a rolling average in y of over 41 grid points, and in z of 7 grid points is taken. To avoid the impact of the internal wave forcing, a rolling wave average is taken over one wave period as well. For the smallest h_w, as well as for the subcritical cases, this averaging is not enough, and we are unable to extract the impact of the mixing events from the regular wave patterns. Hence, these results are not included in Fig. 12b. For each time step, and each vertical profile, we find all the indices for the negative values of $N^{2\prime}$, above the same slope cutoff described in the previous section. Intervals of consecutive indices indicate the vertical extent of the stratification anomaly. The full range of a well-mixed intrusion will also include small positive regions on either side of the negative anomaly. To capture these, the first positive peak in stratification anomaly on either side of the negative range is taken to be the end points of the intrusion. An example of such a profile with the measured intrusions can be seen in Fig 11(c). After averaging over all the calculated thicknesses at a given time step, we again average in time over the last 4 waves (rolling wave average removes the last wave as a possibility) to find an average intrusion thickness for each simulation.

References

Armi, L., 1978: Some evidence for boundary mixing in the deep ocean. *Journal of Geophysical Research*, **83**, 1971, https://doi.org/10.1029/JC083iC04p01971.

Aucan, J., M. A. Merrifield, D. A. Luther, and P. Flament, 2006: Tidal mixing events on the deep flanks of kaena ridge, hawaii. *Journal of Physical Oceanography*, **36**, https://doi.org/10.1175/JPO2888.1.

Balmforth, N. J., and W. R. Young, 2002: Tidal conversion by subcritical topography. *Journal of Physical Oceanography*, **32**, 2900–2914.

Bonnin, J., H. van Haren, P. Hosegood, and G.-J. A. Brummer, 2006: Burst resuspension of seabed material at the foot of the continental slope in the rockall channel. *Marine Geology*, **226**, 167–184, https://doi.org/10.1016/j.margeo.2005.11.006.

Cacchione, D. A., and D. E. Drake, 1986: Nepheloid layers and internal waves over continental shelves and slopes. *Geo-Marine Letters*, **6**, https://doi.org/10.1007/BF02238085.

Chalamalla, V. K., B. Gayen, A. Scotti, and S. Sarkar, 2013: Turbulence during the reflection of internal gravity waves at critical and near-critical slopes. *Journal of Fluid Mechanics*, **729**, 47–68, https://doi.org/10.1017/jfm.2013.240.

Cheriton, O. M., E. E. McPhee-Shaw, W. J. Shaw, T. P. Stanton, J. G. Bellingham, and C. D. Storlazzi, 2014: Suspended particulate layers and internal waves over the southern monterey bay continental shelf: An important control on shelf mud belts? *Journal of Geophysical Research: Oceans*, **119**, https://doi.org/10.1002/2013JC009360.

Churchill, J. H., P. E. Biscaye, and F. Aikman, 1988: The character and motion of suspended particulate matter over the shelf edge and upper slope off cape cod. *Continental Shelf Research*, **8**, https://doi.org/10.1016/0278-4343(88)90077-5.

Cyr, F., and H. van Haren, 2016: Observations of small-scale secondary instabilities during the shoaling of internal bores on a deep-ocean slope. *Journal of Physical Oceanography*, **46**, 219–231, https://doi.org/10.1175/JPO-D-15-0059.1.

Dillon, T. M., 1982: Vertical overturns: A comparison of thorpe and ozmidov length scales. *Journal of Geophysical Research*, **87**, https://doi.org/10.1029/jc087ic12p09601.

Drake, H. F., R. Ferrari, and J. Callies, 2020: Abyssal circulation driven by near-boundary mixing: Water mass transformations and interior stratification. *Journal of Physical Oceanography*, **50**, 2203–2226, https://doi.org/10.1175/JPO-D-19-0313.1.

Drazin, P. G., 1961: On the steady flow of a fluid of variable density past an obstacle. *Tellus*, **13**, 239–251, https://doi.org/10.1111/j.2153-3490.1961.tb00081.x.

Edge, W. C., N. L. Jones, M. D. Rayson, and G. N. Ivey, 2021: Calibrated suspended sediment observations beneath large amplitude non-linear internal waves. *Journal of Geophysical Research: Oceans*, **126**, https://doi.org/10.1029/2021JC017538.

Eriksen, C. C., 1985: Implications of ocean bottom reflection for internal wave spectra and mixing. *Journal of Physical Oceanography*, **15**, https://doi.org/10.1175/1520-0485(1985)015⟨1145:ioobrf⟩2.0.co;2.

Ferrari, R., A. Mashayek, T. J. McDougall, M. Nikurashin, and J. M. Campin, 2016: Turning ocean mixing upside down. *Journal of Physical Oceanography*, **46**, https://doi.org/10.1175/JPO-D-15-0244.1.

Gardner, W. D., B. E. Tucholke, M. J. Richardson, and P. E. Biscaye, 2017: Benthic storms, nepheloid layers, and linkage with upper ocean dynamics in the western north atlantic. *Marine Geology*, **385**, 304–327, https://doi.org/10.1016/j.margeo.2016.12.012.

Garrett, C., P. Maccready, and P. Rhines, 1993: Boundary mixing and arrested ekman layers: Rotating stratified flow near a sloping boundary. *Annu. Rev. Fluid Mech*, **25**, 291–323.

Gayen, B., and S. Sarkar, 2011: Boundary mixing by density overturns in an internal tidal beam. *Geophysical Research Letters*, **38**, https://doi.org/10.1029/2011GL048135.

Holmes, R. M., and T. J. McDougall, 2020: Diapycnal transport near a sloping bottom boundary. *Journal of Physical Oceanography*, **50**, https://doi.org/10.1175/JPO-D-20-0066.1.

Hopfinger, E. J., 1987: Turbulence in stratified fluids: A review. *Journal of Geophysical Research*, **92**, 5287, https://doi.org/10.1029/JC092iC05p05287.

Jalali, M., V. K. Chalamalla, and S. Sarkar, 2017: On the accuracy of overturn-based estimates of turbulent dissipation at rough topography. *Journal of Physical Oceanography*, **47**, 513–532, https://doi.org/10.1175/JPO-D-15-0169.1.

Kaiser, B. E., L. J. Pratt, and J. Callies, 2022: Low-reynolds-number oscillating boundary layers on adiabatic slopes. *Journal of Fluid Mechanics*, **950**, A4, https://doi.org/10.1017/jfm.2022.794.

Khani, S., 2018: Mixing efficiency in large-eddy simulations of stratified turbulence. *Journal of Fluid Mechanics*, **849**, 373–394, https://doi.org/10.1017/jfm.2018.417.

Klymak, J. M., S. Legg, M. H. Alford, M. Buijsman, R. Pinkel, and J. D. Nash, 2012: The direct breaking of internal waves at steep topography. *Oceanography*, **25**, 153–159, https://doi.org/10.5670/oceanog.2012.50.

Kunze, E., C. Mackay, E. E. Mcphee-Shaw, K. Morrice, J. B. Girton, and S. R. Terker, 2012: Turbulent mixing and exchange with interior waters on sloping boundaries. *Journal of Physical Oceanography*, **42**, 910–927, https://doi.org/10.1175/JPO-D-11-075.1.

Lamb, K. G., 2014: Internal wave breaking and dissipation mechanisms on the continental slope/shelf. *Annual Review of Fluid Mechanics*, **46**, 231–254, https://doi.org/10.1146/annurev-fluid-011212-140701.

Legg, S., and J. Klymak, 2008: Internal hydraulic jumps and overturning generated by tidal flow over a tall steep ridge. *Journal of Physical Oceanography*, **38**, 1949–1964, https://doi.org/10.1175/2008JPO3777.1.

Lu, Y. Z., X. R. Cen, S. X. Guo, L. Qu, P. Q. Huang, X. D. Shang, and S. Q. Zhou, 2021: Spatial variability of diapycnal mixing in the south china sea inferred from density overturn analysis. *Journal of Physical Oceanography*, **51**, https://doi.org/10.1175/JPO-D-20-0241.1.

Marshall, J., D. Jamous, and J. Nilsson, 1999: Reconciling thermodynamic and dynamic methods of computation of water-mass transformation rates. *Deep Sea Research I*, **46**, 545–572.

Mashayek, A., R. Ferrari, S. Merrifield, J. R. Ledwell, L. S. Laurent, and A. N. Garabato, 2017: Topographic enhancement of vertical turbulent mixing in the southern ocean. *Nature Communications*, **8**, 14 197, https://doi.org/10.1038/ncomms14197.

McPhee-Shaw, E., 2006: Boundary–interior exchange: Reviewing the idea that internal-wave mixing enhances lateral dispersal near continental margins. *Deep Sea Research Part II: Topical Studies in Oceanography*, **53**, 42–59, https://doi.org/10.1016/j.dsr2.2005.10.018.

McPhee-Shaw, E. E., and E. Kunze, 2002: Boundary layer intrusions from a sloping bottom: A mechanism for generating intermediate nepheloid layers. *Journal of Geophysical Research*, **107**, https://doi.org/10.1029/2001jc000801.

McPhee-Shaw, E. E., E. Kunze, and J. B. Girton, 2021: Submarine canyon oxygen anomaly caused by mixing and boundary-interior exchange. *Geophysical Research Letters*, **48**, https://doi.org/10.1029/2021GL092995.

Nielson, J. R., and S. M. Henderson, 2022: Bottom boundary layer mixing processes across internal seiche cycles: Dominance of downslope flows. *Limnology and Oceanography*, **67**, 1111–1125, https://doi.org/10.1002/lno.12060.

Nokes, R. L., and G. N. Ivey, 1989: Vertical mixing due to the breaking of critical internal waves on sloping boundaries. *Journal of Fluid Mechanics*, **204**, https://doi.org/10.1017/S0022112089001849.

Petruncio, E. T., L. K. Rosenfeld, and J. D. Paduan, 1997: Observations of the internal tide in monterey canyon. *Journal of Physical Oceanography*.

Polzin, K. L., J. M. Toole, J. R. Ledwell, and R. W. Schmitt, 1997: Spatial variability of turbulent mixing in the abyssal ocean. *Science*, **276**, 93–96.

Ramadhan, A., and Coauthors, 2020: Oceananigans.jl: Fast and friendly geophysical fluid dynamics on gpus. *Journal of Open Source Software*, **5**, 2018, https://doi.org/10.21105/joss.02018.

Reynolds, W. C., and A. K. Hussain, 1972: The mechanics of an organized wave in turbulent shear flow. part 3. theoretical models and comparisons with experiments. *Journal of Fluid Mechanics*, **54**, https://doi.org/10.1017/S0022112072000679.

Ruan, X., and R. Ferrari, 2023: Diapycnal upwelling driven by tidally-induced mixing over steep topography. [preprint]. 239–251.

Sarkar, S., and A. Scotti, 2017: From topographic internal gravity waves to turbulence. *Annual Review of Fluid Mechanics*, **49**, 195–220, https://doi.org/10.1146/annurev-fluid-010816-060013.

Scorer, R. S., 1949: Theory of waves in the lee of mountains. *Quarterly Journal of the Royal Meteorological Society*, **75**, 41–56, https://doi.org/10.1002/qj.49707532308.

Slinn, D. N., and J. J. Riley, 1998: Theoretical and computational fluid dynamics turbulent dynamics of a critically reflecting internal gravity wave 1. *Theoret. Comput. Fluid Dynamics*, **11**, 281–303.

Thorpe, S., and M. White, 1988: A deep intermediate nepheloid layer. *Deep Sea Research Part A. Oceanographic Research Papers*, **35 (9)**, 1665–1671, https://doi.org/https://doi.org/10.1016/0198-0149(88)90109-4.

Thorpe, S. A., 1977: Turbulence and mixing in a scottish loch. *Philosophical Transactions of the Royal Society of London*, **286**, 125–181.

van Haren, H., 2006: Nonlinear motions at the internal tide source. *Geophysical Research Letters*, **33**, 2006GL025 851, https://doi.org/10.1029/2006GL025851.

van Haren, H., 2023: Kmt, detailing layered mixing governed by internal wave breaking. *Environmental Fluid Mechanics*, **23**, 603–620, https://doi.org/10.1007/s10652-023-09921-5.

van Haren, H., A. Cimatoribus, and L. Gostiaux, 2015: Where large deep-ocean waves break. *Geophysical Research Letters*, **42**, 2351–2357, https://doi.org/10.1002/2015GL063329.

van Haren, H., and L. Gostiaux, 2012a: Detailed internal wave mixing above a deep-ocean slope. *Journal of Marine Research*, **70**, 173–197.

van Haren, H., and L. Gostiaux, 2012b: Energy release through internal wave breaking. *Oceanography*, **25**, 124–131, https://doi.org/10.5670/oceanog.2012.47.

Winters, K. B., 2015: Tidally driven mixing and dissipation in the stratified boundary layer above steep submarine topography. *Geophysical Research Letters*, **42**, 7123–7130, https://doi.org/10.1002/2015GL064676.

Winters, K. B., and L. Armi, 2013: The response of a continuously stratified fluid to an oscillating flow past an obstacle. *Journal of Fluid Mechanics*, **727**, 83–118, https://doi.org/10.1017/jfm.2013.247.

Wynne-Cattanach, B., and Coauthors, 2023: Observational evidence of diapycnal upwelling within a sloping submarine canyon. *Pre Print. Research Square*, https://doi.org/10.21203/rs.3.rs-3459062/v1.